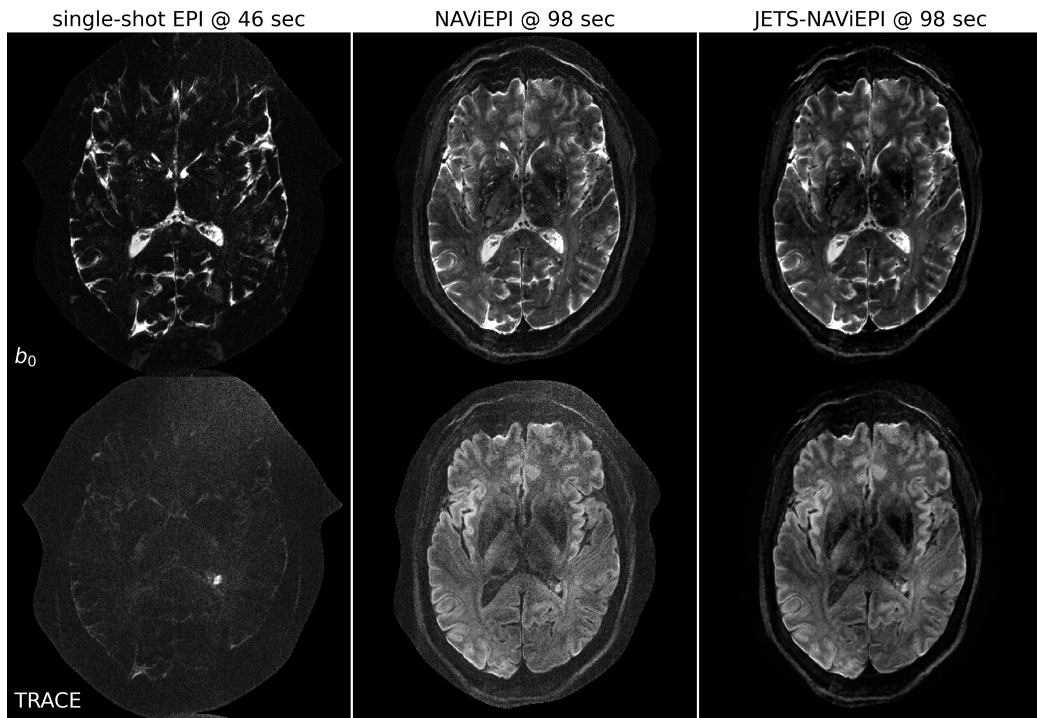


## Graphical Abstract

### Accelerated Diffusion Weighted Magnetic Resonance Imaging at 7 T: Joint Reconstruction for Shift-Encoded Navigator-based Interleaved Echo Planar Imaging (JETS-NAViEPI)

Zhengguo Tan, Patrick Alexander Liebig, Robin Martin Heidemann, Frederik Bernd Laun, Florian Knoll

**3-scan trace acquisition with voxel size 0.5 X 0.5 X 2.0 mm<sup>3</sup>**



## Highlights

### **Accelerated Diffusion Weighted Magnetic Resonance Imaging at 7 T: Joint Reconstruction for Shift-Encoded Navigator-based Interleaved Echo Planar Imaging (JETS-NAViEPI)**

Zhengguo Tan, Patrick Alexander Liebig, Robin Martin Heidemann, Frederik Bernd Laun, Florian Knoll

- Navigator-based interleaved EPI acquisition with minimal distortion mismatch between echoes
- Novel accelerated diffusion acquisition with shifted phase encoding among diffusion directions for complementary  $k$ - $q$ -space sampling at 7 T
- Generalized joint  $k$ - $q$ -slice diffusion-weighted image reconstruction with overlapping locally low-rank regularization
- Efficient simultaneous multi-slice (SMS) image reconstruction
- 3-scan trace acquisition with the voxel size  $0.5 \times 0.5 \times 2.0 \text{ mm}^3$  and 60 slices at 1.5 min

# Accelerated Diffusion Weighted Magnetic Resonance Imaging at 7 T: Joint Reconstruction for Shift-Encoded Navigator-based Interleaved Echo Planar Imaging (JETS-NAViEPI)

Zhengguo Tan<sup>a</sup>, Patrick Alexander Liebig<sup>b</sup>, Robin Martin Heidemann<sup>b</sup>,  
Frederik Bernd Laun<sup>c</sup>, Florian Knoll<sup>a</sup>

<sup>a</sup>*Department Artificial Intelligence in Biomedical Engineering (AIBE),  
Friedrich-Alexander University of Erlangen-Nuremberg, Erlangen, Germany*

<sup>b</sup>*Siemens Healthcare GmbH, Erlangen, Germany*

<sup>c</sup>*Institute of Radiology, University Hospital Erlangen, Friedrich-Alexander University of Erlangen-Nuremberg, Erlangen, Germany*

---

## Abstract

The pursuit of high spatial-angular-temporal resolution for in vivo diffusion-weighted magnetic resonance imaging (DW-MRI) at ultra-high field strength (7 T and above) is important in understanding brain microstructure and function. Such pursuit, however, faces several technical challenges. First, increased off-resonance and shorter  $T_2$  relaxation require faster echo train readouts. Second, existing high-resolution DW-MRI techniques usually employ in-plane fully-sampled multi-shot EPI, which not only prolongs the scan time but also induces a high specific absorption rate (SAR) at 7 T. To address these challenges, we develop in this work navigator-based interleaved EPI (NAViEPI) which enforces the same effective echo spacing (ESP) between the imaging and the navigator echo. First, NAViEPI renders no distortion mismatch between the two echoes, and thus simplifies shot-to-shot phase variation correction. Second, NAViEPI allows for a large number of shots

(e.g.  $> 4$ ) with undersampled iEPI acquisition, thereby rendering clinically-feasible high-resolution sub-millimeter protocols. To retain signal-to-noise ratio (SNR) and to reduce undersampling artifacts, we developed the  $k_y$ -shift encoding among diffusion encodings to explore complementary  $k$ - $q$ -space sampling. Moreover, we developed a novel joint reconstruction with overlapping locally low-rank regularization generalized to the multi-band multi-shot acquisition at 7 T (dubbed JETS-NAViEPI). R1.6

*Keywords:* Diffusion-weighted magnetic resonance imaging, Echo planar imaging, Navigator, Ultra-high field, Joint reconstruction, Low rank, Simultaneous multi slice

---

<sup>1</sup> **1. Introduction**

<sup>2</sup> Diffusion-weighted magnetic resonance imaging (DW-MRI) ([Le Bihan et al., 1986; Merboldt et al., 1985](#)) is a non-invasive modality that is sensitive to the intravoxel Brownian motion of water molecules. DW-MRI forms the basis for diffusion tensor imaging (DTI) ([Basser et al., 1994; Mori et al., 1999](#)) and high angular resolution diffusion imaging (HARDI) ([Tuch et al., 2002](#)), and has been widely used in acute brain ischemia diagnosis, in tumor detection and staging, and in neuroscience ([Jones, 2010](#)).

<sup>9</sup> For DW-MRI acquisition, the commonly used pulse sequence is single-shot echo-planar imaging (SS-EPI) ([Mansfield, 1977](#)). SS-EPI is capable of rapidly acquiring one DW image per radio-frequency excitation at the order of 100 ms, and is thus motion robust. However, conventional SS-EPI, even with three-fold accelerated acquisition ([Bammer et al., 2001](#)) using parallel imaging ([Roemer et al., 1990; Ra and Rim, 1993; Pruessmann et al., 1999; Griswold et al., 2002](#)), still suffers from low spatial resolution and geometric distortions.

<sup>17</sup> In the quest for high spatial-angular-temporal-resolution and minimal-geometric-distortion DW-MRI, tremendous efforts have been made. Techniques on the correction of image distortions induced by off-resonances and eddy currents have been developed ([Andersson et al., 2003](#)). Furthermore, gSlider ([Setsompop et al., 2018](#)) with blipped-CAIPI ([Setsompop et al., 2012](#)) for simultaneous multi-slice (SMS) ([Maudsley, 1980; Breuer et al., 2005](#)) was proposed to achieve high-resolution DW-MRI. Advanced pulse sequences based on [multi-shot EPI](#) have also been developed, including but not limited to interleaved EPI (iEPI) ([Butts et al., 1993](#)), PROPELLER ([Pipe et al., 2002](#)), R3.7, R3.8 R3.15

26 and readout-segmented EPI (rsEPI) (Porter and Heidemann, 2009; Heide-  
27 mann et al., 2010).

28 Based on four-shot iEPI, multiplexed sensitivity encoding (MUSE) image  
29 reconstruction achieved DW-MRI with a sub-millimeter in-plane resolution  
30 and maximal  $b$ -value  $800 \text{ s/mm}^2$  at 3 T (Chen et al., 2013). The four-shot  
31 iEPI employed in MUSE acquired an in-plane fully-sampled  $k$ -space, except  
32 partial Fourier. Every shot (segment), corresponding to four-fold under-  
33 sampling, was then reconstructed via parallel imaging to obtain shot-to-shot  
34 phase variation. This indicates that increasing the number of shots in MUSE  
35 will result in higher undersampling per shot, and consequently, degrade shot  
36 phase estimation (Wu and Miller, 2017). On the other hand, the use of in-  
37 plane fully-sampled four-shot iEPI is challenging at ultra-high field (e.g. 7 T),  
38 because the SAR is linearly proportional to the square of the field strength.

39 Alternatively, navigator-based iEPI acquisition has been proposed (Jeong  
40 et al., 2013; Dai et al., 2017, 2018). These proposals may allow for a larger  
41 number of shots, and hence higher spatial resolution. However, due to the use  
42 of different ESP between the imaging echo and the navigator echo, these pro-  
43 posals suffered from geometric distortion mismatch between the two echoes  
44 and thus required specific compensation methods. In contrast, rsEPI (Porter  
45 and Heidemann, 2009; Heidemann et al., 2010) used the same readout seg-  
46 ment for both echoes, and thus required no correction of the navigator echo.

47 Beyond the MUSE-type parallel imaging reconstruction, compressed sens-  
48 ing (Lustig et al., 2007; Block et al., 2007) has been explored. For instance,  
49 multi-shot reconstruction techniques based on structured low-rank matrix  
50 completion (MUSSELS) (Mani et al., 2017; Bilgic et al., 2019) achieved 5-

shot DW-MRI with 9-fold undersampling per shot. Recently, JULEP (Dai et al., 2023) incorporated explicit phase mapping into MUSSELS. These reconstruction techniques, i.e., MUSE, MUSSELS and JULEP, targeted the reconstruction of one DW image from interleaved EPI acquisition, and did not explore joint- $k$ - $q$ -space undersampling or reconstruction.

Joint- $k$ - $q$ -space undersampling can be achieved via proper regularization along the diffusion encoding direction. Relevant examples are diffusion undersampling with Gaussian process estimated reconstruction (DAGER) (Wu et al., 2019) and magnitude-based spatial-angular locally low-rank regularization (SPA-LLR) (Hu et al., 2020). However, DAGER addressed the reconstruction problem of single-shot EPI acquisition. SPA-LLR focused on the reconstruction of single-band and fully-sampled iEPI acquisition.

In this work, we propose a Joint  $k$ - $q$ -slice rEconsTruction framework for Shift-encoded NAVigator-based interleaved EPI at 7 T (dubbed JETS-NAViEPI). Our pulse sequence, NAViEPI, differs from most existing techniques. First, NAViEPI builds upon interleaved EPI, thereby allowing for fast and efficient  $k$ -space coverage. Second, inspired by rsEPI, NAViEPI ensures the same effective ESP between the imaging and the navigator echo, thereby minimizing geometric distortion and allowing for the use of a larger number of shots. NAViEPI essentially integrates the advantages of both iEPI and rsEPI. Third, NAViEPI utilizes undersampled multi-shot iEPI, thereby alleviating the SAR problem at 7 T. Fourth, NAViEPI shifts the  $k$ -space in-plane sampling pattern along the phase encoding ( $k_y$ ) direction. This shifting creates complementary  $k$ - $q$ -space sampling, which leads to the possibility of our joint  $k$ - $q$ -slice reconstruction. Specifically, we employ spatial-diffusion

<sup>76</sup> overlapping LLR regularization to jointly reconstruct all diffusion encodings  
<sup>77</sup> and multi-band slices. In vivo experiments at 7 T and comparisons with other  
<sup>78</sup> techniques demonstrate the efficiency of our proposed method in achieving  
<sup>79</sup> high spatial resolution DW-MRI at ultra-high field.

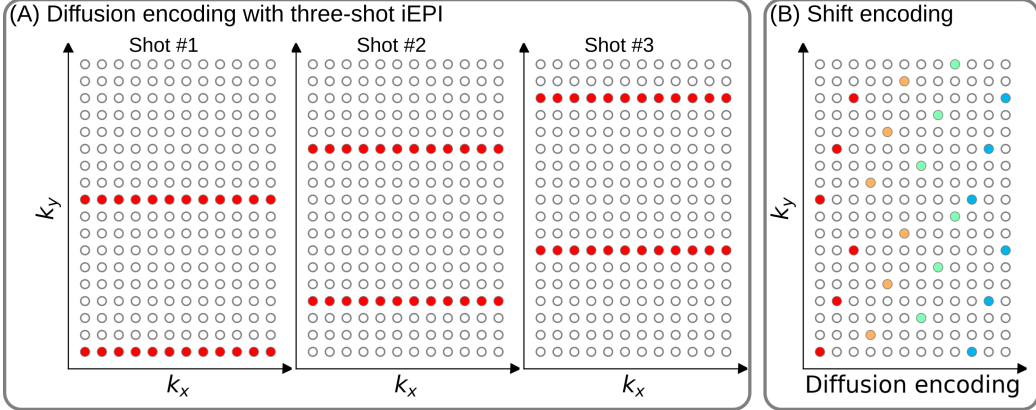


Figure 1: (A) An example DW-MRI acquisition with three-shot interleaved EPI acquisition. (B) The proposed  $k_y$  shifted diffusion encoding scheme. This example employs three shots per DW image. Therefore, every three columns have the same color.

## 80 2. Materials and methods

### 81 2.1. Multi-band shift-encoded iEPI acquisition

82 Fig. 1 (A) displays the diffusion-weighted image acquisition based on  
 83 three-shot interleaved EPI with three-fold in-plane undersampling. Conven-  
 84 tionally, such a sampling pattern is repeated for all diffusion directions. In  
 85 contrast, we propose the  $k_y$ -shifted diffusion encoding, as shown in Fig. 1 (B).  
 86 The interleaved EPI sampling pattern is shifted by one  $k_y$  line per diffusion  
 87 direction, with the cycling period being the in-plane undersampling factor.

88 It is worth noting that, as shown in Fig. 1 (A), the undersampling factor  
 89 of one segment is  $R_{\text{in-plane}} \times N_{\text{shot}}$  (ignore multi-band undersampling here),  
 90 yielding nine-fold in-plane undersampling in this example. In other words,  
 91 the undersampling factor per segment linearly scales up with the number  
 92 of shots. Consequently, conventional self-gating reconstruction techniques,  
 93 e.g. MUSE, suffer from degraded shot-to-shot phase estimation, which in

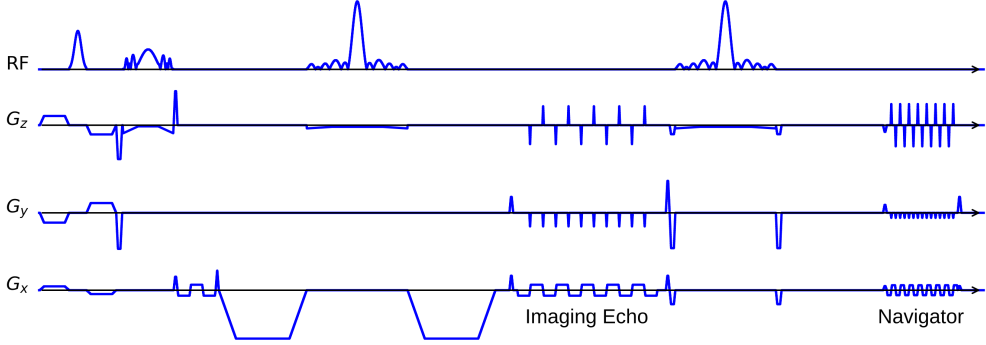


Figure 2: The NAViEPI sequence diagram. SMS is utilized for the acquisition of both imaging and navigator echoes. While the acceleration factor per navigator is the same as listed in Table 1, the acceleration factor per imaging echo is in addition linearly scaled by the number of shots.

94 turn limits the number of shots and spatial resolution.

95 *2.2. NAViEPI: Navigator-based iEPI with consistent effective ESP between  
96 the imaging and the navigator echo - where iEPI meets rsEPI*

97 Instead of the self-gated MUSE with in-plane fully-sampled iEPI and  
98 a limited number of shots, We propose NAVigator-based interleaved EPI  
99 (NAViEPI), as illustrated in Fig. 2. Moreover, inspired by rsEPI (Porter and  
100 Heidemann, 2009), NAViEPI enforces a consistent effective ESP between the  
101 imaging and the navigator echo, thereby minimizing distortion mismatch  
102 between the two echoes.

103 Since one imaging echo presents one segment in multi-shot EPI acquisi-  
104 tion, its effective ESP is defined as

$$\text{ESP}_{\text{eff}} = \frac{\text{ESP}}{R_{\text{in-plane}} \times N_{\text{shot}}} \quad (1)$$

105 Here, a larger number of shots (segments) increases the undersampling factor  
106 per segment (see Fig. 1), but decreases the effective ESP. Since the navigator

107 echo is acquired for each segment, its in-plane undersampling factor equals  
108  $R_{\text{in-plane}}$ . Therefore, the effective ESP of the navigator echo must match that  
109 of the imaging echo, as given in Eq. (1). With a matching effective ESP, the  
110 base resolution of the navigator echo can then be determined.

111 *2.3. In vivo acquisition protocols*

112 We implemented multiple in-vivo acquisition protocols at a clinical 7 T  
113 MR system (MAGNETOM Terra, Siemens Healthineers, Erlangen, Ger-  
114 many) equipped with a 32-channel head coil (Nova Medical, Wilmington,  
115 MA, USA) and the XR-gradient system (**maximum gradient strength 80 mT/m**  
116 **with a peak slew rate of 200 T/m/s**). To calibrate coil sensitivity maps, refer- R3.22  
117 ence scans employed a gradient-echo (GRE) sequence. Spectral fat saturation  
118 and mono-polar diffusion-encoding gradients were used. The phase-encoding  
119 direction was selected as anterior-to-posterior.

Table 1: NAViEPI acquisition protocols

Protocol	1.0 mm isotropic		sub-millimeter	
	#1	#2	#3	#4
Diffusion mode	MDDW <sup>1</sup>		3-scan trace	
Diffusion scheme			monopolar	
Diffusion direction	20	30	3	
<i>b</i> -value (s/mm <sup>2</sup> )			1000	
<i>b</i> <sub>0</sub>	0			1
Voxel size (mm <sup>3</sup> )		1.0	0.5 × 0.5 × 2.0	
Slices	141	124	60	
FOV (mm <sup>2</sup> )		200	220	
Base resolution		200	440	
Navigator	No	No	Yes	No
Shots	4	2	5	1
TR (ms)	7700	8500	4400	8000
TEs (ms)	67	56	58/95.1	143
ESP (ms)	1.02	1.06	1.52	1.48
Bandwidth (Hz/Pixel)		1086	758	
Partial Fourier		6/8		
Acceleration <sup>2</sup>	1 × 3	3 × 2	3 × 2	
TA (min) <sup>3</sup>	10 : 42	9 : 12	1 : 38	0 : 46

<sup>1</sup> MDDW: Multi-direction diffusion weighting;<sup>2</sup> Acceleration: Both in-plane and slice undersampling can be employed, denoted as ( $R_{\text{in-plane}} \times R_{\text{slice}}$ );<sup>3</sup> TA: Total acquisition time.

121 This study was approved by the local ethics committee. Three volunteers R3.1  
122 with informed consent obtained before scanning participated in this study.  
123 Detailed acquisition protocols are listed in Table 1.

124 *2.3.1. 20-diffusion-direction acquisition at 1.0 mm<sup>3</sup> isotropic resolution*

125 As listed in Table 1, Protocol #1 with six-shot iEPI and without in- R1.1,  
126 plane undersampling was implemented. This protocol represents the acquisi-  
127 tion scheme employed in many existing multi-shot reconstruction techniques,  
128 (e.g., MUSE, SPA-LLR, and JULEP). The acquired data from this protocol R1.1,  
129 served as ground truth. Different reconstruction methods, i.e., JETS, MUSE, R1.2  
130 and JULEP were compared.

131 We then retrospectively reduced the four-shot data to only one shot per R1.1  
132 diffusion encoding without and with the proposed  $k_y$  shifting to simulate  
133 three-fold in-plane undersampling. JETS reconstruction was performed on  
134 all data to validate the proposed  $k_y$ -shifted acquisition.

135 *2.3.2. 30-diffusion-direction acquisition at 1.0 mm<sup>3</sup> isotropic resolution*

136 Protocol #2 in Table 1 was implemented for diffusion tensor imaging R1.1  
137 (DTI) (Basser et al., 1994). Given the use of 30 diffusion encodings, we  
138 reduced the number of shots to two and switched off the navigator such as  
139 to shorten the total scan time. This is reasonable because two segments with  
140 three-fold in-plane undersampling correspond to six-fold undersampling per  
141 segment, which is acceptable for the self-gated phase estimation.

142 *2.3.3. 3-scan trace acquisition at 0.5 × 0.5 × 2.0 mm<sup>3</sup> voxel size*

143 As listed in Table 1, Protocol #3 was implemented based on NAViEPI R1.1  
144 with five shots per diffusion encoding. This protocol was compared against

<sub>145</sub> single-shot EPI (Protocol #4) with the same spatial resolution and acceleration,  
<sub>146</sub> such as to demonstrate the sampling efficiency of NAViEPI.

<sub>147</sub> *2.4. Forward modeling*

<sub>148</sub> Our proposed acquisition method yields multi-dimensional **multi-band**  
<sub>149</sub> *k*-space data  $\mathbf{y}_{c,q,s}$ , where  $c, q, s$  denotes the index of the coil sensitivity  
<sub>150</sub> map, the diffusion encoding, and the shot, respectively. **Acquisition model-**  
<sub>151</sub> **ing needs to consider several aspects.** R1.25  
<sub>152</sub> R1.26

<sub>152</sub> First, the acquired *k*-space data  $\mathbf{y}$  is mapped from individual shot images  
<sub>153</sub>  $\mathbf{x}_{q,s,z}$  via the forward model,

$$\mathbf{y}_{c,q,s} = \mathbf{P}_{q,s} \boldsymbol{\Sigma} \boldsymbol{\Theta}_z \mathbf{F} \mathbf{S}_c \mathbf{x}_{q,s,z}$$

$$\mathbf{y} := \mathbf{E}_1 \mathbf{x} \quad (2)$$

<sub>154</sub> Here, the encoding matrix  $\mathbf{E}_1$  comprises a chain of linear operators. Every  
<sub>155</sub> shot image  $\mathbf{x}$  is point-wise multiplied by a set of coil sensitivity maps ( $\mathbf{S}$ ) and  
<sub>156</sub> Fourier transformed ( $\mathbf{F}$ ). The output is then point-wise multiplied by the  
<sub>157</sub> multi-slice phase map ( $\boldsymbol{\Theta}$ ) with  $z$  the slice index in simultaneously excited  
<sub>158</sub> slices. This operator shifts individual slice along the phase-encoding direction  
<sub>159</sub> via varying phase modulation (Breuer et al., 2005). The SMS *k*-space data  
<sub>160</sub> is then summed (collapsed,  $\boldsymbol{\Sigma}$ ) along the slice dimension and masked (point-  
<sub>161</sub> wise multiplied,  $\mathbf{P}$ ) by the sampling pattern of **each** diffusion encoding and  
<sub>162</sub> shot. R1.27

<sub>163</sub> Second, for diffusion MRI based on multi-shot EPI, **multiple shots ac-**  
<sub>164</sub> **quired for a given** diffusion encoding need to be combined as one DW image R1.28  
<sub>165</sub> ( $\tilde{\mathbf{x}}$ ). A possibility is to perform magnitude average (Chen et al., 2013) or R1.29

166 root-sum-squares (RSS) (Mani et al., 2017) of shot images. This method  
 167 is robust to in-plane motion, but sub-optimal concerning SNR (Guhaniyogi R3.27  
 168 et al., 2016). Alternatively, shot combination can be done via shot-to-shot R1.30  
 169 phase variation correction (Liu et al., 2005; Chen et al., 2013). This can  
 170 be incorporated to our formulation as point-wise multiplication between the R1.31  
 171 shot-to-shot phase variation ( $\Phi$ ) and the DW image ( $\tilde{\mathbf{x}}$ ),

$$\mathbf{x}_{q,s,z} = \Phi_{q,s,z} \tilde{\mathbf{x}}_{q,z} \quad (3)$$

172 Note that  $\tilde{\mathbf{x}}$  can be obtained by applying the adjoint of  $\Phi$  to  $\mathbf{x}$ . In MUSE,  
 173  $\Phi$  is obtained by parallel imaging reconstruction of all shots with subsequent  
 174 phase smoothing of every shot image. Based on this phase correction, the  
 175 complete forward model follows

$$\mathbf{y} := \mathbf{E}_2 \tilde{\mathbf{x}} = \mathbf{E}_1 \Phi \tilde{\mathbf{x}} \quad (4)$$

176 where the encoding matrix  $\mathbf{E}_2$  comprises the chain of the shot-to-shot phase  
 177 variation  $\Phi$  and the encoding matrix  $\mathbf{E}_1$ . We implemented these two encoding  
 178 matrices in SigPy (Ong and Lustig, 2019).

### 179 2.5. Joint $k$ - $q$ -slice reconstruction

180 Based on the generalized forward models in Eqs. (2) and (4), our proposed  
 181 joint  $k$ - $q$ -slice reconstruction can be formulated as a three-step approach.

182 **I. Navigator echo reconstruction.** The acquisition of navigator echoes  
 183 follows the forward model in Eq. (2), so the reconstruction of navigator  
 184 echoes can be formulated as:

$$\operatorname{argmin}_{\mathbf{x}} \|\mathbf{y} - \mathbf{E}_1 \mathbf{x}\|_2^2 + \lambda \mathbf{R}(\mathbf{x}) \quad (5)$$

185 where  $\mathbf{R}(\mathbf{x})$  denotes the regularization functional with the regularization  
 186 strength  $\lambda$ . In this work,  $\ell^2$  regularization was used, i.e.,  $\mathbf{R}(\mathbf{x}) =$   
 187  $\|\mathbf{x}\|_2^2$ . In the case of self-navigating (i.e., no navigator acquired) as Pro-  
 188 tocol #2, the central  $k$ -space region (i.e., 1/4 of the full image matrix)  
 189 of each segment is used as  $\mathbf{y}$  in Eq. (5).

190 **II. Iterative phase smoothing.** Shot-to-shot phase variation was ex-  
 191 tracted from the reconstructed navigator echo phases. Assuming that R1.13  
 192 phase images are spatially smooth (Chen et al., 2013; Dai et al., 2023),  
 193 we employed the iterative approach to smooth phase,

$$\mathbf{x}^{(k+1)} = \mathbf{F}^{-1} \mathcal{H} \mathbf{F} \mathbf{x}^{(k)} \quad (6)$$

194 where the index  $k$  denotes the iteration, and  $x^{(0)}$  is then the recon-  
 195 structed navigator image from Step I.  $\mathcal{H}$  is the Hanning window.

196 **III. Shot-combined reconstruction.** Joint reconstruction of all DW im-  
 197 ages using the shot-combined forward model  $\mathbf{E}_2$  with shot-to-shot phase  
 198 variation from Step II reads:

$$\operatorname{argmin}_{\tilde{\mathbf{x}}} \|\mathbf{y} - \mathbf{E}_2 \tilde{\mathbf{x}}\|_2^2 + \lambda \|\mathbf{T} \tilde{\mathbf{x}}\|_* \quad (7)$$

199 Here, LLR regularization was employed in the local spatial-diffusion  
 200 matrices, based on the theory of partially separable functions (Liang, R1.35  
 201 2007; Trzasko and Manduca, 2011; Zhang et al., 2015).  $\mathbf{T}$  represents a  
 202 linear operator that firstly slides a local patch window through all DW  
 203 images and then flattens every set of local patches to two-dimensional R1.36  
 204 (2D) matrices, comprising spatial and diffusion dimensions. The nuclear  
 205 norm regularization is enforced via singular value thresholding (SVT)

of all flattened 2D matrices (Cai et al., 2010). We implemented this regularization term as a proximal operator (Beck, 2017). R3.28

This work employed blipped-CAIPI SMS (Setsompop et al., 2012), in which spatially separated slices are simultaneously excited and acquired. Therefore, 2D instead of 3D patches were used to construct the spatial-diffusion matrices. R1.14

It has been reported that LLR is prone to checkerboard artifacts when  $\lambda$  is too large (Hu et al., 2020). We overcame this problem by utilizing overlapping blocks and providing an efficient implementation. If the blocks overlap,  $\mathbf{T}^H \mathbf{T}$  input  $\neq$  input, where  $\mathbf{T}^H$  denotes the Hermitian adjoint operator of  $\mathbf{T}$ . This is because overlapping values are summed in the output of  $\mathbf{T}^H$ . Our efficient implementation was to scale  $\mathbf{T}^H$  as  $(1/\text{divisor})\mathbf{T}^H$ , where the divisor matrix was obtained by  $\mathbf{T}^H \mathbf{T} \mathbf{1} \cdot \mathbf{1}$  denoted the matrix of all ones with the same shape as the input. R3.11, R3.30  
R3.31

## 2.6. Reconstruction

The acquired raw data was read in by twixtools (<https://github.com/pehses/twixtools>). Ramp-sampling regridding and FOV/2-ghost correction were also performed in twixtools. Subsequently, coil sensitivity maps were computed from reference scans using ESPIRiT (Uecker et al., 2014) in SigPy (Ong and Lustig, 2019).

With this pre-processing as well as the implemented forward models and proximal operator, the inverse problem in Eq. (7) was solved by the alternating direction method of multipliers (ADMM) (Boyd et al., 2010). R1.39

229 ADMM solves the minimization problems in an alternating update scheme,

$$\begin{cases} \mathbf{x}^{(k+1)} := \underset{\mathbf{x}}{\operatorname{argmin}} \| \mathbf{y} - \mathbf{E}(\mathbf{x}) \|^2 + \rho/2 \| \mathbf{T}\mathbf{x} - \mathbf{z}^{(k)} + \mathbf{u}^{(k)} \|_2^2 \\ \mathbf{z}^{(k+1)} := \mathcal{T}_{\lambda/\rho}(\mathbf{T}\mathbf{x}^{(k+1)} + \mathbf{u}^{(k)}) \\ \mathbf{u}^{(k+1)} := \mathbf{u}^{(k)} + \mathbf{T}\mathbf{x}^{(k+1)} - \mathbf{z}^{(k+1)} \end{cases} \quad (8)$$

230 where  $k$  denotes the ADMM iteration.  $\mathbf{z}$  is the auxiliary variable ( $\mathbf{z} = \mathbf{T}\mathbf{x}$ ),  
231 and  $\mathbf{u}$  is the Lagrangian multipliers. Importantly, when solving Eq. (2),  $\mathbf{x}$   
232 denotes shot images and  $\mathbf{E}$  denotes  $\mathbf{E}_1$  in Eq. (8). In contrast,  $\mathbf{x}$  denotes shot-  
233 combined images and  $\mathbf{E}$  denotes  $\mathbf{E}_2$  when solving Eq. (4).  $\mathbf{x}$  can be solved  
234 using linear least square algorithms, e.g. conjugate gradients (Hestenes and R3.35  
235 Stiefel, 1952), while  $\mathbf{z}$  is updated via singular value thresholding ( $\mathcal{T}$ ) with R2.8,  
236 the thresholding parameter  $\lambda/\rho$ . The coupling parameter  $\rho$  is effective in R3.32  
237 both the update of  $\mathbf{x}$  and  $\mathbf{z}$ . It acts as Tikhonov regularization strength  
238 when updating  $\mathbf{x}$ , but also inversely scales the thresholding strength when  
239 updating  $\mathbf{z}$ , as shown in Supporting Information Figures S1 and S2.

240 In this work, 15 ADMM iterations with  $\rho = 0.05$  and  $\lambda = 0.04$ , and a  
241 block size of 6 for LLR (refer to Supporting Information Figure S3) were  
242 used. All reconstructions were done on a single A100 SXM4/NVLink GPU  
243 with 40 GB memory (NVIDIA, Santa Clara, CA, USA). R3.37

244 We compared our proposed joint reconstruction with established multi-  
245 shot reconstruction techniques, specifically, MUSE (Chen et al., 2013) and  
246 JULEP (Dai et al., 2023), hosted on GitHub by Dr. Dai (Dai et al., 2023).  
247 Further, we performed the local-PCA denoising (Cordero-Grande et al., 2019)  
248 as implemented in MRtrix (Tournier et al., 2019) on the MUSE reconstructed  
249 complex DW images. R1.3

250 With reconstructed DW images from Protocol #2 in Table 1, color-coded

251 fractional anisotropy (cFA) maps ([Basser et al., 1994](#)) were fitted using DiPy  
252 ([Garyfallidis et al., 2014](#)),

253 **3. Results**

254 *3.1. Iterative smoothing of shot-to-shot phase variation*

255 Navigators were acquired with the acceleration rate as listed in Table 1.  
256 Besides, the base resolution of navigators (e.g. 32 in Protocol #3 in Table 1)  
257 was smaller than imaging echoes. As a result, reconstructed navigator phases  
258 (refer to the first column in Fig. 3) from Step I in Section 2.5 are not spatially  
259 smooth. Such phases, when used in the shot-combined reconstruction, result  
260 in signal void artifacts in DW images. To address this problem, we utilized  
261 the iterative smoothing procedure. As show in Fig. 3, the ripple-like phase  
262 artifact disapper after five iterations. It can also be seen that such iterative  
263 procedure retains the shot-to-shot phase variation.

264 *3.2. Comparison to MUSE and JULEP with four-shot iEPI acquisition*

265 The iterative phase smoothing was also applicable to MUSE-type self- R1.1,  
266 navigating reconstruction, where shot phases were reconstructed from imag- R1.2  
267 ing echoes. Fig. 4 compares our proposed JETS with MUSE (Chen et al.,  
268 2013), MUSE with complex-valued local-PCA denoiser (Cordero-Grande et al.,  
269 2019), and JULEP (Dai et al., 2023). The residual noise from MUSE can be  
270 largely removed by the denoiser. However, when compared to JETS, the de-  
271 noiser shows residual noise patterns within the globus pallidus (indicated by  
272 the red arrow). JETS also shows better denoising than JULEP. The reason  
273 is that JETS enforces spatial-diffusion regularization, whereas JULEP for-  
274 mulates structured low-rank regularization of the four shots for one diffusion  
275 encoding.

### Iterative smoothing of shot-to-shot phase variation

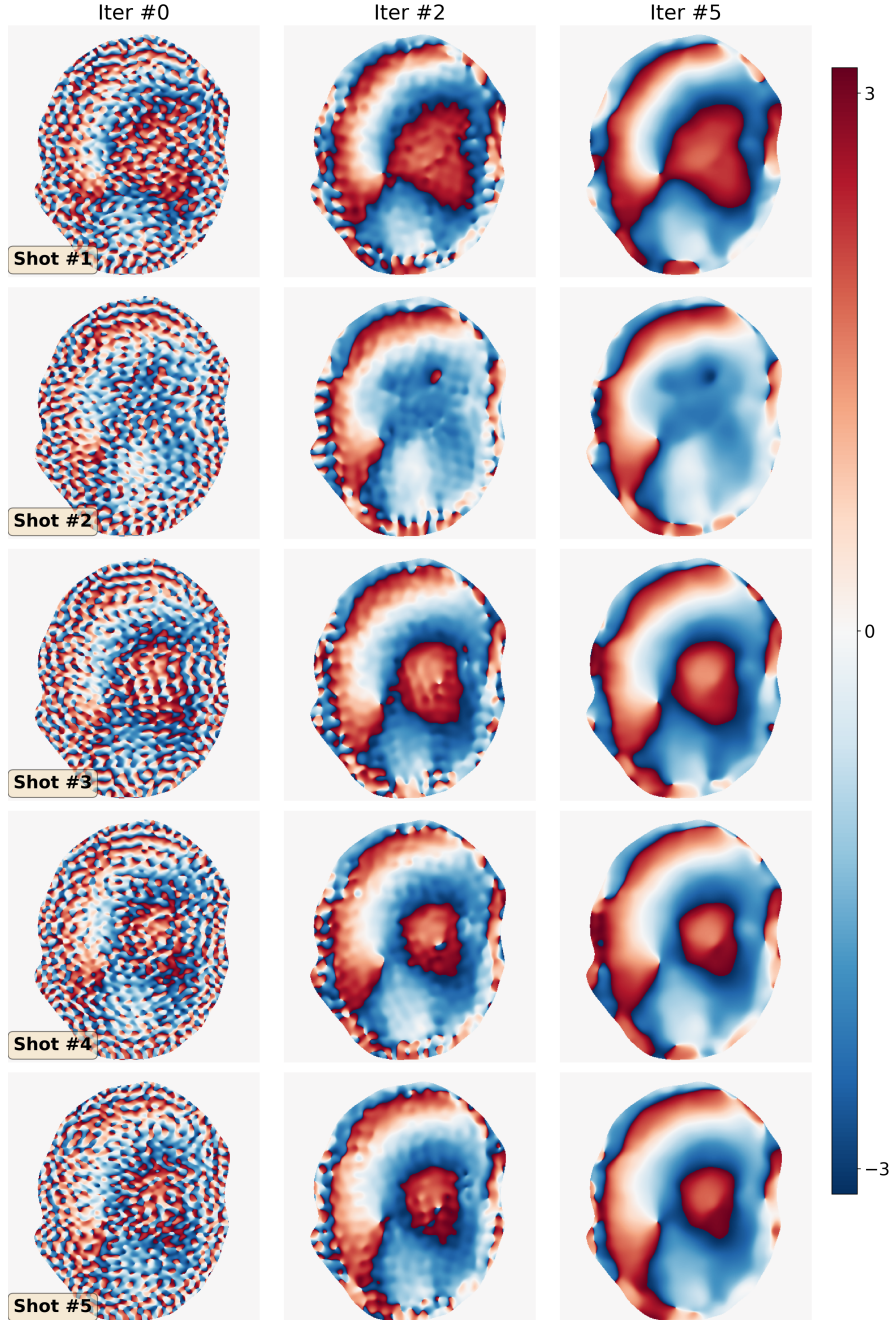


Figure 3: Iterative smoothing of shot-to-shot phase variation according to Eq. (6). Navigators from Protocol #3 were reconstructed based on Step I in Section 2.5 and then used as the input (iter #0, left column).

**8th DW image from 4-shot iEPI @ 1 mm ISO**

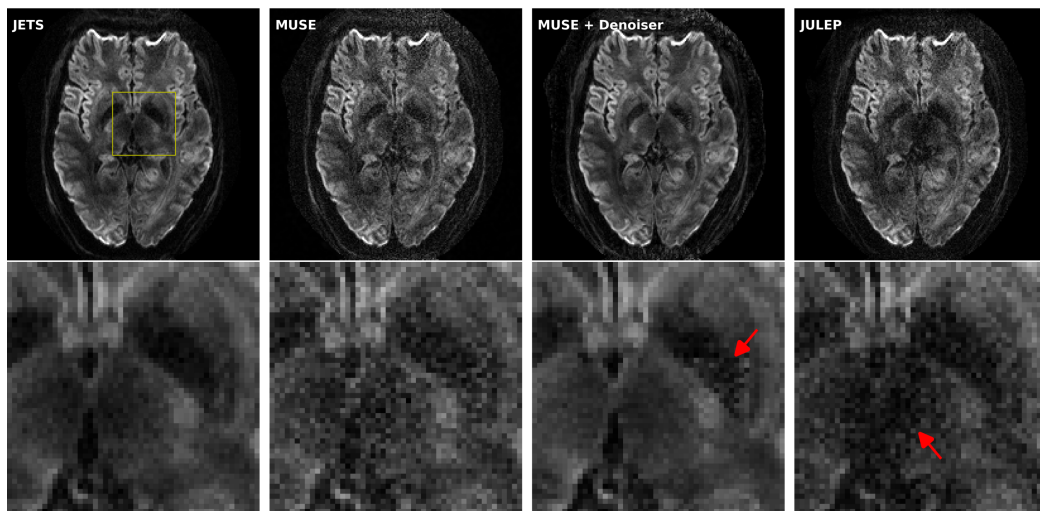


Figure 4: Reconstructed DW images (the 8th diffusion encoding) based on 4-shot iEPI acquisition with 1 mm isotropic resolution (Protocol #1 in Table 1). Four reconstruction methods are compared (from left to right): JETS, MUSE, MUSE with denoiser, and JULEP. The 2nd row displays the magnified views of the yellow square.

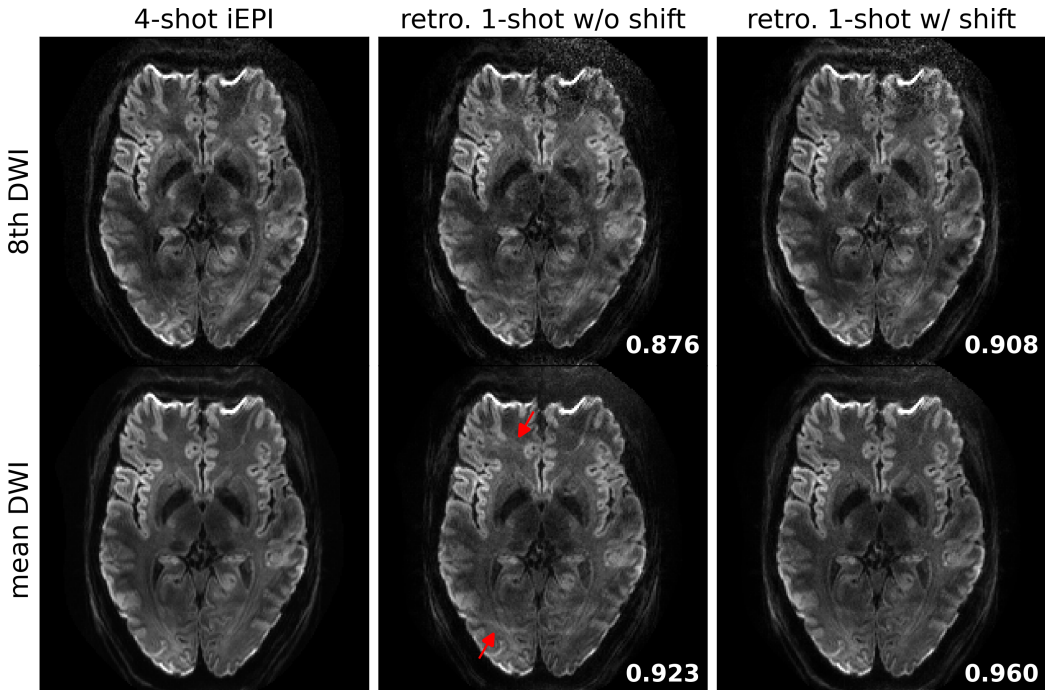


Figure 5: Quantitative validation of the proposed  $k_y$ -shift encoding sampling pattern based on 4-shot iEPI acquisition with 1 mm isotropic resolution (Protocol #1 in Table 1). (Top) the 8th diffusion encoding and (bottom) mean DWI over 20 diffusion encodings. (1st column) JETS reconstruction of 4-shot iEPI acquisition is used as the ground truth. The 2nd and the 3rd column displays JETS reconstruction of retrospectively undersampled 1-shot acquisition without and with  $k_y$  shifting, respectively. structural similarity (SSIM) values are computed and displayed in the bottom right corners.

276    3.3. *Retrospectively undersampling from the four-shot iEPI acquisition*

277    JETS reconstruction results on the four-shot prospectively fully-sampled R1.1  
278    data from Protocol #1 in Table 1, as well as on the retrospectively under-  
279    sampled one-shot data without and with the proposed  $k_y$  shift are displayed  
280    in Fig. 5. Residual aliasing artifacts are visible in the reconstruction without  
281     $k_y$  shifting, as pointed by the red arrows. On the contrary, the reconstruction  
282    with the proposed  $k_y$  shifting among diffusion encodings shows much reduced  
283    aliasing, reduced noise, and higher SSIM.

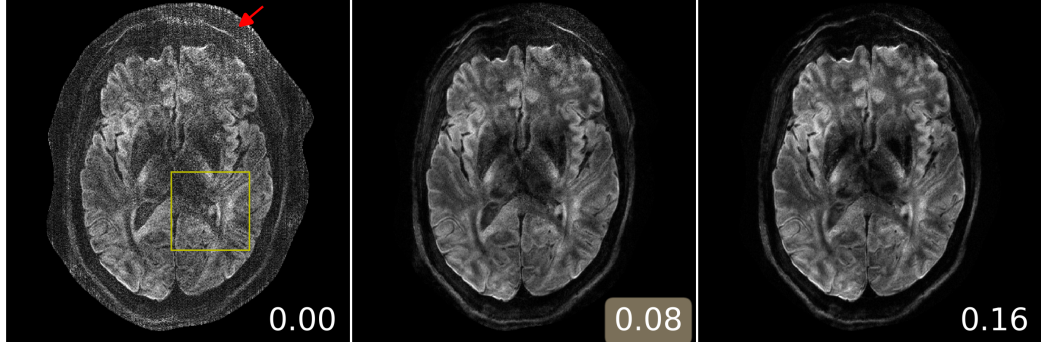
284    3.4. *Analysis of reconstruction parameters*

285    Here we provide a systematic analysis of the proposed JETS reconstruc- R1.4  
286    tion with LLR regularization applied to the spatial-diffusion dimension, as  
287    shown in Fig. 6.

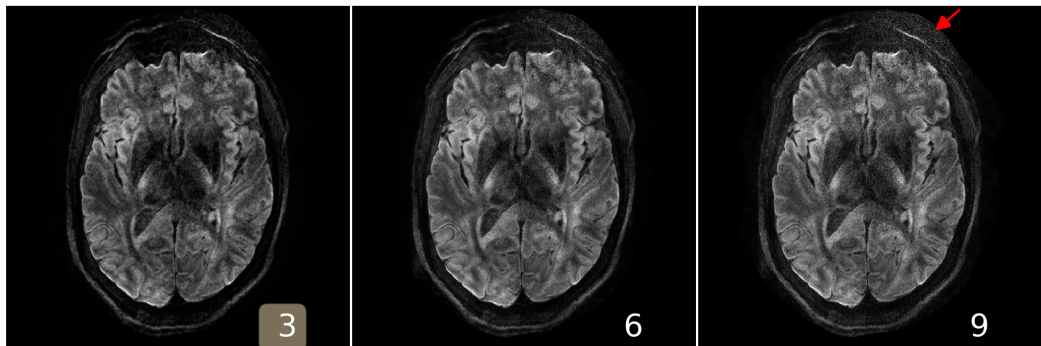
288    First, we varied the regularization strength  $\lambda$  from 0, to 0.08, and to  
289    0.16. The reconstruction with  $\lambda = 0$  in Eq. (7) corresponds to parallel  
290    imaging reconstruction without LLR regularization. It is worth noting that  
291    the proposed NAViEPI sequence demonstrates high-quality sub-millimeter  
292    DW images ( $0.5 \times 0.5 \times 2.0 \text{ mm}^3$  in this example). The DW images can be  
293    further improved with the use of LLR regularization, i.e., reduced noise, as  
294    seen in the reconstruction with  $\lambda = 0.08$ . Increasing  $\lambda$  (e.g. 0.16) further  
295    reduces noise, but at the cost of increased blurring. Therefore,  $\lambda = 0.08$  was  
296    selected in this work.

297    Second, besides the regularization strength, the block size (i.e., the width  
298    of square 2D patches) also plays a role in denoising. Here, the block size of 3  
299    shows the best denoising as compared to 6 and 9, especially in the peripheral  
300    brain region. According to (Cordero-Grande et al., 2019), it is suggested

**(A) varying  $\lambda$ , keeping block as 6 and stride as 1**



**(B) varying block size, keeping  $\lambda$  as 0.08 and stride as 1**



**(C) varying stride, keeping  $\lambda$  as 0.08 and block as 6**

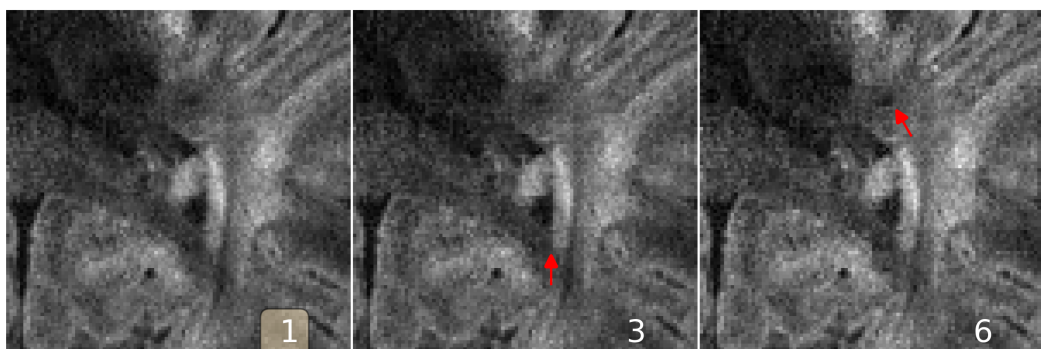


Figure 6: Analysis of reconstruction parameters based on the 3-scan trace acquisition with  $0.5 \times 0.5 \times 2.0 \text{ mm}^3$  (Protocol #3 in Table 1). Displayed are JETS reconstructed single-direction DW images. **(A)** Varying the regularization strength  $\lambda$  from 0 to 0.08 and 0.16. **(B)** Varying the block size from 3 to 6 and 9. **(C)** Varying the stride size from 1 to 3 and 6 (non-overlapping).

301 to keep the patch size roughly equal to the diffusion encoding length. In  
302 this 3-scan trace acquisition example, the diffusion encoding length is 4 (1  $b_0$   
303 plus 3 orthogonal diffusion directions). Among the tested block sizes, 3 is the  
304 closest to 4, and hence renders better denoising, whereas the other block sizes  
305 may require stronger regularization strength. In practice, we also observed  
306 that smaller block sizes construct smaller matrices for SVT and thus lead to  
307 shorter computation time.

308 Third, we varied the stride, i.e., the increment from one local patch to  
309 the next. When the block size equals the stride (6 in this example), it refers  
310 to non-overlapping LLR, which is prone to checkerboard artifacts even with  
311 the use of random shifting ([Saucedo et al., 2017](#)) in each ADMM iteration,  
312 as indicated by the red arrows in the magnified views of Fig. 6. Therefore,  
313 we utilized the overlapping LLR with the stride of 1, which requires the  
314 implementation of the scaling matrix in Section 2.5 to avoid the summation  
315 of overlapped pixels. The drawback of overlapping LLR, however, is the  
316 increased number of matrices for SVT and hence the increased computation  
317 time ([Saucedo et al., 2017](#)).

318 *3.5. Sampling efficiency of NAViEPI*

319 As shown in Fig. 7, NAViEPI achieves sub-millimeter resolution (voxel R3.5  
320 size  $0.5 \times 0.5 \times 2.0 \text{ mm}^3$ ) with the use of 5-shot acquisition. When compared  
321 to the single-shot acquisition with the same voxel size, the acquisition time  
322 of NAViEPI is about two times longer, but the image quality of NAViEPI is  
323 remarkably improved.

324 In the sub-millimeter imaging scenario, the increased base resolution re-  
325 quires longer TE (143 ms) in the single-shot acquisition, which results in

**3-scan trace acquisition with voxel size  $0.5 \times 0.5 \times 2.0 \text{ mm}^3$**

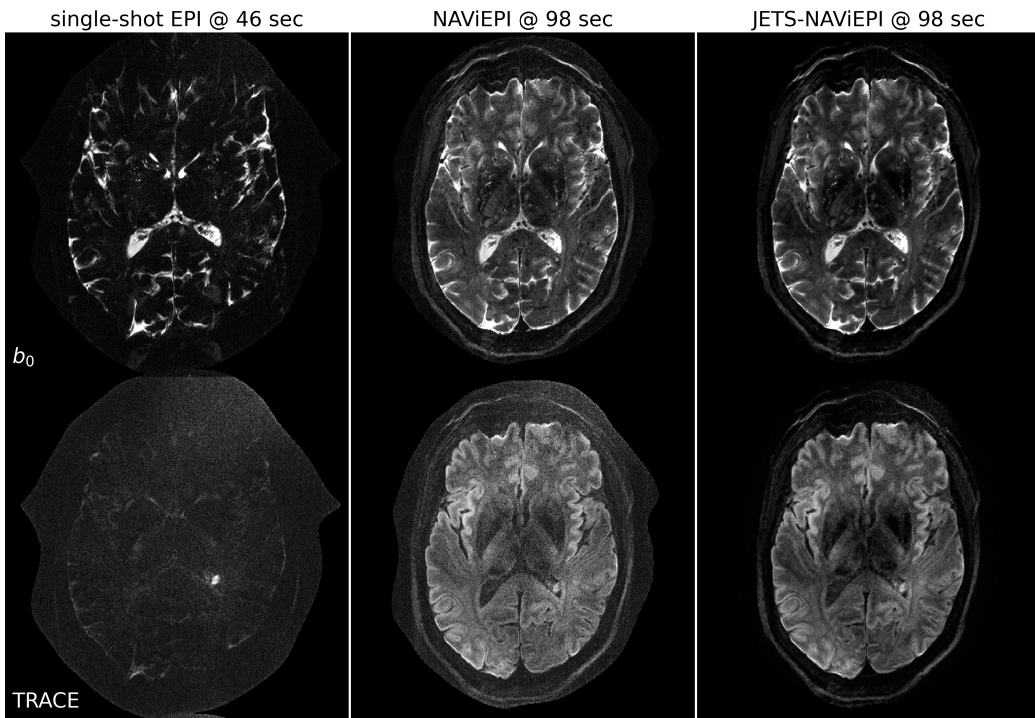


Figure 7: Sampling efficiency of the proposed NAViEPI sequence. 5-shot NAViEPI acquisition with the voxel size  $0.5 \times 0.5 \times 2.0 \text{ mm}^3$  (Protocol #3) was compared with single-shot EPI acquisition (Protocol #4). Both the 1st and the 2nd columns were reconstructed via parallel imaging without LLR regularization, whereas the 3rd column was reconstructed via JETS.

**3-scan trace acquisition with voxel size  $0.5 \times 0.5 \times 2.0 \text{ mm}^3$**

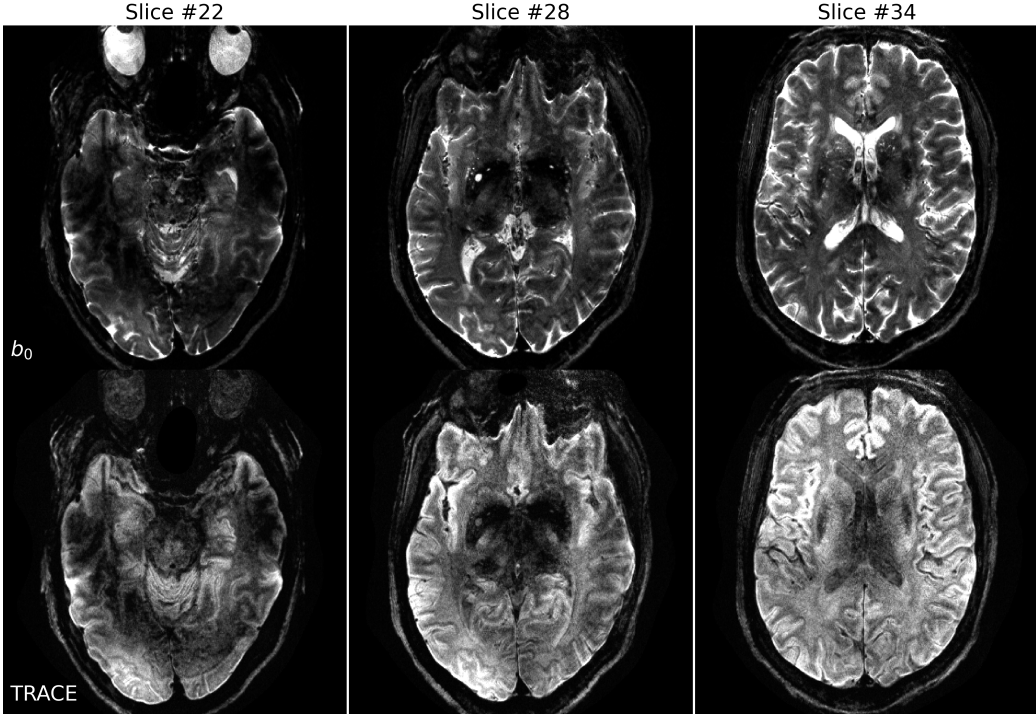


Figure 8: Reconstruction of the 3-scan trace acquisition with the voxel size  $0.5 \times 0.5 \times 2.0 \text{ mm}^3$  (Protocol #3) at different slices.

326 significant signal loss due to  $T_2$  relaxation. Therefore, sub-millimeter DWI  
327 necessitates multi-shot acquisition, which is subject to shot-to-shot phase  
328 variation and long scan time. However, NAViEPI solves both challenges. The  
329 5-shot acquisition reduces TE to 58 ms, and thus retains SNR significantly  
330 compared to the single-shot acquisition. Moreover, the JETS reconstruction  
331 can help to reduce noise and improve structural visibility.

332 Fig. 8 shows the JETS reconstructed  $b_0$  and TRACE images in different R1.7  
333 slice locations. Admittedly, the lower brain region (e.g. slice #22) exhibits in-  
334 homogeneous and lower signal intensity than the upper slices. Such inhomogeneity

335 geneity can be alleviated with the use of multi-channel parallel transmission  
336 (Katscher et al., 2003; Grissom et al., 2010).

337 *3.6. Diffusion tensor imaging*

338 Since 30 diffusion encodings were acquired in Protocol #2, the block size  
339 in LLR regularization was lifted to 6, such that the spatial-diffusion matrix  
340 for SVT has similar width and height. The other parameter were kept the  
341 same as found in Fig. 6.

342 The mean DWIs in Fig. 9 illustrate high spatial resolution and high SNR.  
343 In line with Fig. 8, we can notice the signal loss in the cerebellum region, due  
344 to the use of single-channel transmission in this work. On the other hand,  
345 the reconstructed cFA maps in Fig. 9 show clear fiber orientation in all ori-  
346 entations. Moreover, tiny fiber structures can be visualized in the zoomed-in  
347 cFA maps. Because of the low signal sensitivity surrounding the cerebellum,  
348 residual artifacts are visible in the zoomed-in sagittal view. To enhance the  
349 DTI fitting performance, one possibility is to acquire more diffusion encod-  
350 ings.

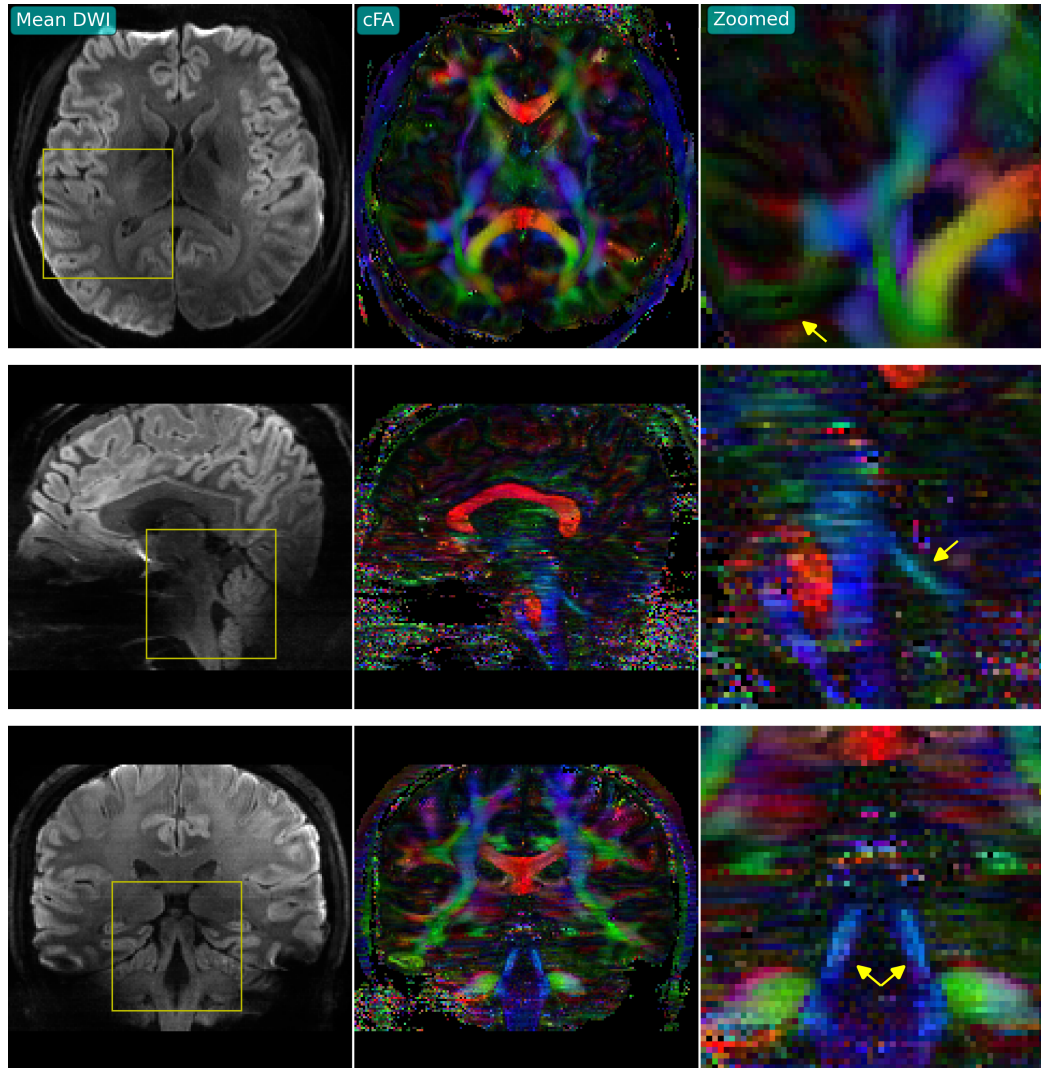


Figure 9: (Left) Mean DWI, (middle) cFA, and (right) cFA in the zoomed-in region based on JETS reconstructed DWI from Protocol #2. Three orthogonal slices (transversal, sagittal, and coronal) are displayed from top to bottom.

351    4. Discussion

352    This work reports a novel DW-MRI technique, JETS-NAViEPI. NAViEPI  
353    (1) achieves the fast and efficient acquisition of both imaging and navigator  
354    echoes, (2) enforces consistent effective ESP between the two echoes, and (3)  
355    allows for undersampled iEPI as well as a large number of shots. Moreover,  
356    compared to the single-shot acquisition, joint  $k$ - $q$ -slice reconstruction with  
357     $k_y$ -shift encoding on NAViEPI retains SNR and reduces aliasing artifacts  
358    in DW images. As a result, JETS-NAViEPI renders high spatiotemporal  
359    resolution diffusion MRI protocols in 7 T, e.g., 3-scan trace acquisition with  
360    the voxel size  $0.5 \times 0.5 \times 2.0 \text{ mm}^3$  at 1.5 min.

361    One limitation of JETS-NAViEPI is the long reconstruction time due to R3.48  
362    the simultaneous reconstruction of all DW images and the use of overlapping  
363    locally low-rank regularization. The reconstruction for the Protocol #3 in  
364    Table 1 on an A100 GPU takes about 2 min per multi-band slice. To reduce R3.48  
365    the computation time, coil compression algorithms (Buehrer et al., 2007;  
366    Huang et al., 2008) can be employed to reduce the number of coils for image  
367    reconstruction. Moreover, one may deploy multi-GPU distributed computing  
368    or modern optimization algorithms (e.g. stochastic gradient descent) (Ong  
369    et al., 2020) to speed up the reconstruction.

370    Neither the signal modeling in Eqs. (2) and (4) nor the LLR regulariza- R1.5  
371    tion considers the subject motion. In the presence of motion, the regularized  
372    reconstruction may degrade. To overcome this problem, scout-informed mo-  
373    tion estimation and reconstruction (Polak et al., 2022) could be integrated  
374    into the framework.

375    Another potential extension of this work is to incorporate distortion cor-

376 rection. The standard distortion correction method is known as TOPUP  
377 (Andersson et al., 2003), which acquires two scans with opposing phase-en-  
378 coding directions to obtain the field inhomogeneity map and then performs  
379 conjugate phase reconstruction to correct for distortion.

380 This work employed a single regularization weight  $\lambda$  to enforce low rank-  
381 ness along the spatial-diffusion direction. However, SNR may be heteroge-  
382 neous within the FOV. Therefore, one single regularization scalar may be  
383 inadequate to cover the whole FOV. Beyond this SVT-based machine-learn-  
384 ing reconstruction, one may seek to learn a  $q$ -space prior as the regularizer  
385 (Hammernik et al., 2018; Lam et al., 2019; Mani et al., 2021).

386 Although NAViEPI employs navigators for the acquisition of shot-to- R1.13  
387 shot phase variation, it is worth noting that phase behavior depends on  
388 several hard-to-control factors such as pulsatile motion, bulk motion, loca-  
389 tions within the brain, and diffusion sensitization strength. Therefore, more  
390 comprehensive modeling or post-processing such as image registration may  
391 be considered in future work.

392 While this work reconstructs all DW images and then performs model  
393 fitting, an alternative approach is to directly estimate  $b_0$  and diffusion tensors  
394 from measured  $k$ - $q$ -space data using model-based reconstruction (Knoll et al.,  
395 2015; Dong et al., 2018; Shafieizargar et al., 2023). Compared to DW image  
396 reconstruction, model-based reconstruction solves for a fewer number of un- R3.49  
397 knows, but requires strict diffusion tensor modeling and the use of nonlinear  
398 least square solvers.

399 **5. Conclusions**

400 We demonstrated the JETS-NAViEPI technique, which integrates a  $k_y$ -  
401 shifted encoding interleaved EPI sequence and a joint reconstruction with  
402 overlapping locally low-rank regularization for high spatial-angular-temporal  
403 resolution DW-MRI at 7 T. This technique allows for high-quality DW image  
404 reconstruction with accelerated acquisitions.

405 **Funding**

406 This work was supported by Deutsche Forschungsgemeinschaft (DFG) –  
407 Project Number 513220538, as well as National Institutes of Health (NIH)  
408 R01 EB024532 and P41 EB017183.

409 **Data and code available statement**

410 In the spirit of reproducible and open science, we publish our source  
411 code (<https://github.com/ZhengguoTan/sigpy>) as well as the raw  $k$ -space  
412 data (<https://doi.org/10.5281/zenodo.7548595>). We also provide inter-  
413 active demonstrations of the reconstruction procedure ([https://github.com/ZhengguoTan/demo\\_jets\\_diffusion\\_mri\\_7t](https://github.com/ZhengguoTan/demo_jets_diffusion_mri_7t)).  
414

415 **Acknowledgments**

416 The authors gratefully acknowledge the scientific support and HPC re-  
417 sources provided by the Erlangen National High Performance Computing  
418 Center (NHR@FAU) of Friedrich-Alexander-Universität Erlangen-Nürnberg  
419 (FAU) under the NHR project b143dc. NHR funding is provided by federal

420 and Bavarian state authorities. NHR@FAU hardware is partially funded by  
421 the German Research Foundation (DFG) – 440719683.

422 The authors thank Dr. Peter Neher for the discussion on MITK-Diffusion. R1.2  
423 The authors thank Dr. Berkin Bilgic for making the MUSSELS source code  
424 (<https://bit.ly/2QgBg9U>) publically available, Dr. Erpeng Dai for sharing  
425 the JULEP source code (<https://github.com/daiep/JULEP>) on GitHub,  
426 and Dr. Zhiyong Zhang for sharing the SPA-LLR source code (<https://github.com/ZZgroupSJTU/PMcmsDTI>) on GitHub. The authors also thank  
427 Dr. Philipp Ehses for the discussion on the use of twixtools (<https://github.com/pehses/twixtools>).  
428

430 **References**

431 Andersson, J.L.R., Skare, S., Ashburner, J., 2003. How to correct suscepti-  
432 bility distortions in spin-echo echo-planar images: application to diffusion  
433 tensor imaging. NeuroImage 20, 870–888. doi:[10.1016/S1053-8119\(03\)00336-7](https://doi.org/10.1016/S1053-8119(03)00336-7).  
434

435 Bammer, R., Keeling, S.L., Augustin, M., Pruessmann, K.P., Wolf, R., Stoll-  
436 berger, R., Hartung, H.P., Fazekas, F., 2001. Improved diffusion-weighted  
437 single-shot echo-planar imaging (EPI) in stroke using sensitivity encoding  
438 (SENSE). Magn. Reson. Med. 46, 548–554. doi:[10.1002/mrm.1226](https://doi.org/10.1002/mrm.1226).

439 Basser, P.J., Mattiello, J., Le Bihan, D., 1994. MR diffusion tensor  
440 spectroscopy and imaging. Biophys. J. 66, 259–267. doi:[10.1016/S0006-3495\(94\)80775-1](https://doi.org/10.1016/S0006-3495(94)80775-1).  
441

- <sup>442</sup> Beck, A., 2017. First-order methods in optimization. Society for In-  
<sup>443</sup> dustrial and Applied Mathematics, Philadelphia, PA. doi:[10.1137/1.9781611974997](https://doi.org/10.1137/1.9781611974997).
- <sup>445</sup> Bilgic, B., Chatnuntawech, I., Manhard, M.K., Tian, Q., Liao, C., Iyer, S.S.,  
<sup>446</sup> Cauley, S.F., Huang, S.Y., Polimeni, J.R., Wald, L.L., Setsompop, K.,  
<sup>447</sup> 2019. Highly accelerated multishot echo planar imaging through synergistic  
<sup>448</sup> machine learning and joint reconstruction. Magn. Reson. Med. 82, 1343–  
<sup>449</sup> 1358. doi:[10.1002/mrm.27813](https://doi.org/10.1002/mrm.27813).
- <sup>450</sup> Block, K.T., Uecker, M., Frahm, J., 2007. Undersampled radial MRI with  
<sup>451</sup> multiple coils. Iterative image reconstruction using a total variation con-  
<sup>452</sup> straint. Magn. Reson. Med. 57, 1186–1098. doi:[10.1002/mrm.21236](https://doi.org/10.1002/mrm.21236).
- <sup>453</sup> Boyd, S., Parikh, N., Chu, E., Peleato, B., Eckstein, J., 2010. Distributed  
<sup>454</sup> optimization and statistical learning via the alternating direction method  
<sup>455</sup> of multipliers. Foundations and Trends in Machine Learning 3, 1–122.  
<sup>456</sup> doi:[10.1561/2200000016](https://doi.org/10.1561/2200000016).
- <sup>457</sup> Breuer, F.A., Blaimer, M., Heidemann, R.M., Mueller, M.F., Griswold, M.A.,  
<sup>458</sup> Jakob, P.M., 2005. Controlled aliasing in parallel imaging results in higher  
<sup>459</sup> acceleration (CAPIRINHA) for multi-slice imaging. Magn. Reson. Med.  
<sup>460</sup> 53, 684–691. doi:[10.1002/mrm.20401](https://doi.org/10.1002/mrm.20401).
- <sup>461</sup> Buehrer, M., Pruessmann, K.P., Boesiger, P., Kozerke, S., 2007. Array com-  
<sup>462</sup> pression for MRI with large coil arrays. Magn. Reson. Med 57, 1131–1139.  
<sup>463</sup> doi:[10.1002/mrm.21237](https://doi.org/10.1002/mrm.21237).

- 464 Butts, K., Riederer, S.J., Ehman, R.L., Thompson, R.M., Jack, C.R., 1993.  
465 Interleaved echo planar imaging on a standard MRI system. Magn. Reson.  
466 Med. 31, 67–72. doi:[10.1002/mrm.1910310111](https://doi.org/10.1002/mrm.1910310111).
- 467 Cai, J.F., Candès, E.J., Shen, Z., 2010. A singular value thresholding  
468 algorithm for matrix completion. SIAM. J. Optim. 20, 1956–1982.  
469 doi:[10.1137/080738970](https://doi.org/10.1137/080738970).
- 470 Chen, N.K., Guidon, A., Chang, H.C., Song, A.W., 2013. A robust multi-  
471 shot scan strategy for high-resolution diffusion weighted MRI enabled by  
472 multiplexed sensitivity-encoding (MUSE). NeuroImage 72, 41–47. doi:[10.1016/j.neuroimage.2013.01.038](https://doi.org/10.1016/j.neuroimage.2013.01.038).
- 473
- 474 Cordero-Grande, L., Christiaens, D., Hutter, J., Price, A.N., Hajnal, J.V.,  
475 2019. Complex diffusion-weighted image estimation via matrix recovery  
476 under general noise models. NeuroImage 200, 391–404. doi:[10.1016/j.neuroimage.2019.06.039](https://doi.org/10.1016/j.neuroimage.2019.06.039).
- 477
- 478 Dai, E., Ma, X., Zhang, Z., Yuan, C., Guo, H., 2017. Simultaneous multislice  
479 accelerated interleaved EPI DWI using generalized blipped-CAIPI acqui-  
480 sition and 3D K-space reconstruction. Magn. Reson. Med. 77, 1593–1605.  
481 doi:[10.1002/mrm.26249](https://doi.org/10.1002/mrm.26249).
- 482
- 483 Dai, E., Mani, M., McNab, J.A., 2023. Multi-band multi-shot diffu-  
484 sion MRI reconstruction with joint usage of structured low-rank con-  
485 straints and explicit phase mapping. Magn. Reson. Med. 89, 95–111.  
486 doi:[10.1002/mrm.29422](https://doi.org/10.1002/mrm.29422).

- 486 Dai, E., Zhang, Z., Ma, X., Dong, Z., Li, X., Xiong, Y., Yuan, C., Guo, H.,  
487 2018. The effects of navigator distortion and noise level on interleaved EPI  
488 DWI reconstruction: a comparison between image- and  $k$ -space method.  
489 Magn. Reson. Med. 80, 2024–2032. doi:[10.1002/mrm.27190](https://doi.org/10.1002/mrm.27190).
- 490 Dong, Z., Dai, E., Wang, F., Zhang, Z., Ma, X., Yuan, C., Guo, H., 2018.  
491 Model-based reconstruction for simultaneous multislice and parallel imag-  
492 ing accelerated multishot diffusion tensor imaging. Med. Phys. 45, 3196–  
493 3204. doi:[10.1002/mp.12974](https://doi.org/10.1002/mp.12974).
- 494 Garyfallidis, E., Brett, M., Amirbekian, B., Rokem, A., van der Walt, S.,  
495 Descoteaux, M., Nimmo-Smith, I., Contributors, D., 2014. DIPY, a library  
496 for the analysis of diffusion MRI data. Front. Neuroinform. 8, 1–17. doi:[10.3389/fninf.2014.00008](https://doi.org/10.3389/fninf.2014.00008).
- 498 Grissom, W.A., Sacolick, L., Vogel, M.W., 2010. Improving high-field MRI  
499 using parallel excitation. Imaging Med. 2, 675–693. doi:[10.2217/IIM.10.62](https://doi.org/10.2217/IIM.10.62).
- 501 Griswold, M.A., Jakob, P.M., Heidemann, R.M., Nittka, M., Jellus, V.,  
502 Wang, J., Kiefer, B., Haase, A., 2002. Generalized autocalibrating par-  
503 tially parallel acquisitions (GRAPPA). Magn. Reson. Med. 47, 1202–1210.  
504 doi:[10.1002/mrm.10171](https://doi.org/10.1002/mrm.10171).
- 505 Guhaniyogi, S., Chu, M.L., Chang, H.C., Song, A.W., Chen, N.K., 2016. Mo-  
506 tion immune diffusion imaging using augmented MUSE for high-resolution  
507 multi-shot EPI. Magn. Reson. Med. 75, 639–652. doi:[10.1002/mrm.25624](https://doi.org/10.1002/mrm.25624).

- 508 Hammernik, K., Klatzer, T., Kobler, E., Recht, M.P., Sodickson, D.K., Pock,  
509 T., Knoll, F., 2018. Learning a variational network for reconstruction of  
510 accelerated MRI data. *Magn. Reson. Med.* 79, 3055–3071. doi:[10.1002/mrm.26977](https://doi.org/10.1002/mrm.26977).
- 512 Heidemann, R.M., Porter, D.A., Anwander, A., Feiweier, T., Heberlein, K.,  
513 Knösche, T.R., Turner, R., 2010. Diffusion imaging in humans at 7 T  
514 using readout-segmented EPI and GRAPPA. *Magn. Reson. Med.* 64, 9–  
515 14. doi:[10.1002/mrm.22480](https://doi.org/10.1002/mrm.22480).
- 516 Hestenes, M.R., Stiefel, E., 1952. Methods of conjugate gradients for solving  
517 linear systems. *J. Res. Natl. Bur. Stand.* 49, 409–436. doi:[10.6028/jres.049.044](https://doi.org/10.6028/jres.049.044).
- 519 Hu, Y., Wang, X., Tian, Q., Yang, G., Daniel, B., McNab, J., Hargreaves, B.,  
520 2020. Multi-shot diffusion-weighted MRI reconstruction with magnitude-  
521 based spatial-angular locally low-rank regularization (SPA-LLR). *Magn.*  
522 *Reson. Med.* 83, 1596–1607. doi:[10.1002/mrm.28025](https://doi.org/10.1002/mrm.28025).
- 523 Huang, F., Vijayakumar, S., Li, Y., Hertel, S., Duensing, G.R., 2008. A soft-  
524 ware channel compression technique for faster reconstruction with many  
525 channels. *Magn. Reson. Imaging* 26, 133–141. doi:[10.1016/j.mri.2007.04.010](https://doi.org/10.1016/j.mri.2007.04.010).
- 527 Jeong, H.K., Gore, J.C., Anderson, A.W., 2013. High-resolution human  
528 diffusion tensor imaging using 2-D navigated multishot SENSE EPI at 7  
529 T. *Magn. Reson. Med.* 69, 793–802. doi:[10.1002/mrm.24320](https://doi.org/10.1002/mrm.24320).

- 530 Jones, D.K., 2010. Diffusion MRI: Theory, methods, and applications. Oxford  
531 University Press. doi:[10.1093/med/9780195369779.001.0001](https://doi.org/10.1093/med/9780195369779.001.0001).
- 532 Katscher, U., Börnert, P., Leussler, C., van den Brink, J.S., 2003. Transmit  
533 SENSE. Magn. Reson. Med. 49, 144–150. doi:[10.1002/mrm.10353](https://doi.org/10.1002/mrm.10353).
- 534 Knoll, F., Raya, J.G., Halloran, R.O., Baete, S., Sigmund, E., Bammer, R.,  
535 Block, T., Otazo, R., Sodickson, D.K., 2015. A model-based reconstruction  
536 for undersampled radial spin-echo DTI with variational penalties on the  
537 diffusion tensor. NMR Biomed 28, 353–366. doi:[10.1002/nbm.3258](https://doi.org/10.1002/nbm.3258).
- 538 Lam, F., Li, Y., Peng, X., 2019. Constrained magnetic resonance spectro-  
539 scopic imaging by learning nonlinear low-dimensional models. IEEE Trans.  
540 Med. Imaging 39, 545–555. doi:[10.1109/TMI.2019.2930586](https://doi.org/10.1109/TMI.2019.2930586).
- 541 Le Bihan, D., Breton, E., Lallemand, D., Grenier, P., Cabanis, E., Laval-  
542 Jeantet, M., 1986. MR imaging of intravoxel incoherent motions: appli-  
543 cation to diffusion and perfusion in neurologic disorders. Radiology 161,  
544 401–407. doi:[10.1148/radiology.161.2.3763909](https://doi.org/10.1148/radiology.161.2.3763909).
- 545 Liang, Z.P., 2007. Spatiotemporal imaging with partially separable functions,  
546 in: 2007 4th IEEE International Symposium on Biomedical Imaging: From  
547 Nano to Macro, pp. 988–991. doi:[10.1109/ISBI.2007.357020](https://doi.org/10.1109/ISBI.2007.357020).
- 548 Liu, C., Moseley, M.E., Bammer, R., 2005. Simultaneous phase cor-  
549 rection and SENSE reconstruction for navigated multi-shot DWI with  
550 non-Cartesian  $k$ -space sampling. Magn. Reson. Med. 54, 1412–1422.  
551 doi:[10.1002/mrm.20706](https://doi.org/10.1002/mrm.20706).

- 552 Lustig, M., Donoho, D., Pauly, J.M., 2007. Sparse MRI: The application of  
553 compressed sensing for rapid MR imaging. Magn. Reson. Med. 58, 1182–  
554 1195. doi:[10.1002/mrm.21391](https://doi.org/10.1002/mrm.21391).
- 555 Mani, M., Jacob, M., Kelley, D., Magnotta, V., 2017. Multi-shot sensitivity-  
556 encoded diffusion data recovery using structured low-rank matrix comple-  
557 tion (MUSSELS). Magn. Reson. Med. 78, 494–507. doi:[10.1002/mrm.26382](https://doi.org/10.1002/mrm.26382).
- 559 Mani, M., Magnotta, V.A., Jacob, M., 2021. qModeL: A plug-and-play  
560 model-based reconstruction for highly accelerated multi-shot diffusion MRI  
561 using learned priors. Magn. Reson. Med. 86, 835–851. doi:[10.1002/mrm.28756](https://doi.org/10.1002/mrm.28756).
- 563 Mansfield, P., 1977. Multi-planar image formation using NMR spin echoes.  
564 J Phys C 10, 55–58. doi:[10.1088/0022-3719/10/3/004](https://doi.org/10.1088/0022-3719/10/3/004).
- 565 Maudsley, A.A., 1980. Multiple-line-scanning spin density imaging. J. Magn.  
566 Reson. 41, 112–126. doi:[10.1016/0022-2364\(80\)90207-3](https://doi.org/10.1016/0022-2364(80)90207-3).
- 567 Merboldt, K.D., Hanicke, W., Frahm, J., 1985. Self-diffusion NMR imag-  
568 ing using stimulated echoes. J. Magn. Reson. 64, 479–486. doi:[10.1016/0022-2364\(85\)90111-8](https://doi.org/10.1016/0022-2364(85)90111-8).
- 570 Mori, S., Crain, B.J., Chacko, V.P., Van Zijl, P.C.M., 1999. Three-  
571 dimensional tracking of axonal projections in the brain by mag-  
572 netic resonance imaging. Ann. Neurol. 45, 265–269. doi:[10.1002/1531-8249\(199902\)45:2<265::AID-ANA21>3.0.CO;2-3](https://doi.org/10.1002/1531-8249(199902)45:2<265::AID-ANA21>3.0.CO;2-3).

- 574 Ong, F., Lustig, M., 2019. SigPy: A Python package for high performance  
575 iterative reconstruction, in: Proceedings of the 27th Annual Meeting of  
576 ISMRM, Montréal, CAN, p. 4819. doi:[10.5281/zenodo.5893788](https://doi.org/10.5281/zenodo.5893788).
- 577 Ong, F., Zhu, X., Cheng, J.Y., Johnson, K.M., Larson, P.E.Z., Vasanawala,  
578 S.S., Lustig, M., 2020. Extreme MRI: Large-scale volumetric dynamic  
579 imaging from continuous non-gated acquisitions. Magn. Reson. Med. 84,  
580 1763–1780. doi:[10.1002/mrm.28235](https://doi.org/10.1002/mrm.28235).
- 581 Pipe, J.G., Farthing, V.G., Forbes, K.P., 2002. Multishot diffusion-weighted  
582 FSE using PROPELLER MRI. Magn. Reson. Med. 47, 42–52. doi:[10.1002/mrm.10014](https://doi.org/10.1002/mrm.10014).
- 583 Polak, D., Splitthoff, D.N., Clifford, B., Lo, W.C., Huang, S.Y., Conklin, J.,  
584 Wald, L.L., Setsompop, K., Cauley, S., 2022. Scout accelerated motion  
585 estimation and reduction (SAMER). Magn. Reson. Med. 87, 163–178.  
586 doi:[10.1002/mrm.28971](https://doi.org/10.1002/mrm.28971).
- 587 Porter, D.A., Heidemann, R.M., 2009. High resolution diffusion-weighted  
588 imaging using readout-segmented echo-planar imaging, parallel imaging  
589 and a two-dimensional navigator-based reacquisition. Magn. Reson. Med.  
590 62, 468–475. doi:[10.1002/mrm.22024](https://doi.org/10.1002/mrm.22024).
- 591 Pruessmann, K.P., Weiger, M., Scheidegger, M.B., Boesiger, P., 1999.  
592 SENSE: Sensitivity encoding for fast MRI. Magn. Reson. Med. 42, 952–  
593 962. doi:[10.1002/\(SICI\)1522-2594\(199911\)42:5<952::AID-MRM16>3.0.CO;2-S](https://doi.org/10.1002/(SICI)1522-2594(199911)42:5<952::AID-MRM16>3.0.CO;2-S).

- 596 Ra, J.B., Rim, C.Y., 1993. Fast imaging using subencoding data sets from  
597 multiple detectors. Magn. Reson. Med. 30, 142–145. doi:[10.1002/mrm.1910300123](https://doi.org/10.1002/mrm.1910300123).
- 599 Roemer, P.B., Edelstein, W.A., Hayes, C.E., Souza, S.P., Mueller, O.M.,  
600 1990. The NMR phased array. Magn. Reson. Med. 16, 192–225. doi:[10.1002/mrm.1910160203](https://doi.org/10.1002/mrm.1910160203).
- 602 Saucedo, A., Lefkimiatis, S., Rangwala, N., Sung, K., 2017. Improved com-  
603 putational efficiency of locally low rank MRI reconstruction using iterative  
604 random patch adjustments. IEEE Trans. Med. Imaging 36, 1209–1220.  
605 doi:[10.1109/TMI.2017.2659742](https://doi.org/10.1109/TMI.2017.2659742).
- 606 Setsompop, K., Fan, Q., Stockmann, J., Bilgic, B., Huang, S., Cauley, S.F.,  
607 Nummenmaa, A., Wang, F., Rathi, Y., Witzel, T., Wald, L.L., 2018. High-  
608 resolution *in vivo* diffusion imaging of the human brain with generalized  
609 slice dithered enhanced resolution: Simultaneous multislice (gSlider-SMS).  
610 Magn. Reson. Med. 79, 141–151. doi:[10.1002/mrm.26653](https://doi.org/10.1002/mrm.26653).
- 611 Setsompop, K., Gagoski, B.A., Polimeni, J.R., Witzel, T., Wedeen, V.J.,  
612 Wald, L.L., 2012. Blipped-controlled aliasing in parallel imaging for si-  
613 multaneous multislice echo planar imaging with reduced *g*-factor penalty.  
614 Magn. Reson. Med. 67, 1210–1224. doi:[10.1002/mrm.23097](https://doi.org/10.1002/mrm.23097).
- 615 Shafieizargar, B., Jeurissen, B., Poot, D.H.J., Klein, S., Van Audekerke,  
616 J., Verhoye, M., den Dekker, A.J., Sijbers, J., 2023. ADEPT: Accurate  
617 diffusion echo-planar imaging with multi-contrast shTs. Magn. Reson.  
618 Med. 89, 396–410. doi:[10.1002/mrm.29398](https://doi.org/10.1002/mrm.29398).

- 619 Tournier, J.D., Smith, R., Raffelt, D., Tabbara, R., Dhollander, T., Pietsch,  
620 M., Christiaens, D., Jeurissen, B., Yeh, C.H., Connelly, A., 2019. MRtrix3:  
621 A fast, flexible and open software framework for medical image processing  
622 and visualisation. NeuroImage 202, 116137. doi:<https://doi.org/10.1016/j.neuroimage.2019.116137>.
- 624 Trzasko, J., Manduca, A., 2011. Local versus global low-rank promotion in  
625 dynamic MRI series reconstruction, in: Proceedings of the 19th Annual  
626 Meeting of ISMRM, Montréal, CAN, p. 4371.
- 627 Tuch, D.S., Reese, T.G., Wiegell, M.R., Makris, N., Belliveau, J.W., Wedeen,  
628 V.J., 2002. High angular resolution diffusion imaging reveals intravoxel  
629 white matter fiber heterogeneity. Magn. Reson. Med. 48, 577–582. doi:[10.1002/mrm.10268](https://doi.org/10.1002/mrm.10268).
- 631 Uecker, M., Lai, P., Murphy, M.J., Virtue, P., Elad, M., Pauly, J.M.,  
632 Vasanawala, S.S., Lustig, M., 2014. ESPIRiT – an eigenvalue approach  
633 to autocalibrating parallel MRI: Where SENSE meets GRAPPA. Magn.  
634 Reson. Med. 71, 990–1001. doi:[10.1002/mrm.24751](https://doi.org/10.1002/mrm.24751).
- 635 Wu, W., Koopmans, P.J., Andersson, J.L., Miller, K.L., 2019. Diffusion  
636 Acceleration with Gaussian process Estimated Reconstruction (DAGER).  
637 Magn. Reson. Med. 82, 107–125. doi:[10.1002/mrm.27699](https://doi.org/10.1002/mrm.27699).
- 638 Wu, W., Miller, K.L., 2017. Image formation in diffusion MRI: A review  
639 of recent technical developments. J. Magn. Reson. Imaging 46, 646–662.  
640 doi:[10.1002/jmri.25664](https://doi.org/10.1002/jmri.25664).

641 Zhang, T., Pauly, J.M., Levesque, I.R., 2015. Accelerated parameter mapping  
642 with a locally low rank constraint. Magn. Reson. Med. 73, 655–661. doi:[10.1002/mrm.25161](#).